# Characterization of 3D Loop Antenna to Overcome the Impact of Small Lateral Misalignment in Wirelessly Powered Intracranial Pressure Monitoring System

M. Waqas A. Khan, Muhammad Rizwan, Lauri Sydänheimo, Toni Björninen, Yahya Rahmat-Samii and Leena Ukkonen

***Abstract*— This paper presents a 3D loop antenna to overcome the impact of small lateral misalignment of the order of 2 mm between the inductively coupled antennas. This work is a continuation of our previously reported work. In our previous work, we have successfully activated the pressure monitoring sensor and performed the pressure readout for an intracranial pressure (ICP) monitoring application. The pressure sensor was activated through wireless inductive near field powering. Measurement showed that there was significant effect on pressure readout accuracy due to small lateral misalignment between the inductively coupled antennas. In this article, we demonstrate that the structural properties of a simple 3D loop antenna help to overcome the pressure readout error caused by small lateral misalignment. We present the design procedure, simulation results and pressure readout measurement of the proposed 3D loop antenna. Moreover, the pressure monitoring system shows maximum improvement of 9 mmHg in pressure readout accuracy with proposed 3D loop antenna.**

***Index Terms*— 3D loop antenna, wireless inductive near field powering, intracranial pressure, and implantable system.**

## I. Introduction

Monitoring of intracranial pressure (ICP) is a continuous and life-saving procedure in various brain diseases and injuries [1]. ICP depends on hydrodynamic and hemodynamic parameters controlled by complex and interlinked physiological mechanisms [2]. Although ICP range limits vary with body posture and age, normal ICP in a supine healthy adult is between 7 and 15 mmHg [3]. There are several invasive and non-invasive methods for monitoring of ICP. However, invasive methods have the risk of infection and non-invasive methods lack in accuracy [4]. Therefore, many researchers have focused in developing a battery-powered [5] or a fully passive [6-8] implant for wireless monitoring of ICP. A battery-powered implant has large size due to the size of the battery and its life-time depends on the life-time of the battery. On the other hand, in a fully passive implant the readout distance is relatively small in comparison with the battery-powered implant because of its zero-power operation.

Recently, we have proposed a wirelessly powered implantable pressure monitoring system [9-10] for wireless monitoring of ICP. The proposed system consists of three main units: an on-body unit, an off-body unit and an in-body unit (implant). Figure 1 (a) shows the block diagram of the proposed system. The implant is inductively coupled to the on-body unit and monitors the pressure through a piezoresistive pressure sensor. The monitored pressure is transmitted towards the off-body unit at industrial–scientific–medical (ISM) band of 2.45 GHz. In [9], we have successfully activated the implant through wireless inductive near field powering and monitored the pressure with an acceptable [11] accuracy of 2 mmHg.

Manuscript received May 9, 2017, revised on September 7, 2017 and accepted on October 19, 2017. This work was supported in part by the Academy of Finland, Jane and Aatos Erkko Foundation and TEKES

M. Waqas A. Khan, Muhammad Rizwan, Lauri Sydänheimo, Toni Björninen and Leena Ukkonen are with BioMediTech Institute and Faculty of Biomedical Sciences and Engineering, Tampere University of Technology, Tampere, Finland (e-mail: {muhammad.khan, muhammad.rizwan, lauri.sydanheimo , toni.bjorninen, leena.ukkonen}@tut.fi).

Yahya Rahmat-Samii is with the University of California, Los Angeles, Los Angeles, CA 90095 USA (email: rahmat@ee.ucla.edu).

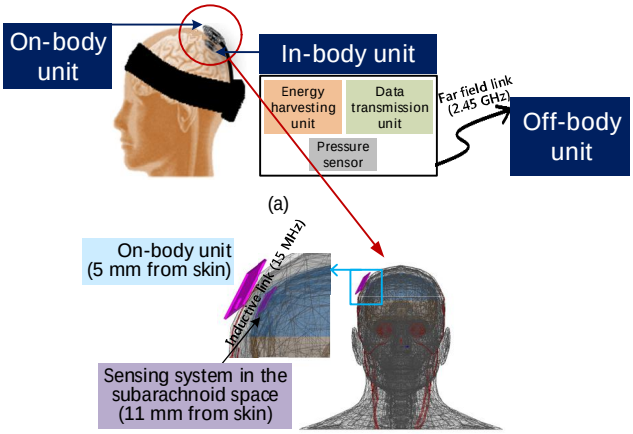


Fig. 1. (a) Functional blocks of the wireless ICP monitoring system. (b) anatomical head model used in the electromagnetic modelling of the inductive power link between the on-body and in-body units. [12]

However, we have also observed that small lateral misalignment of the order of 2 mm between the inductively coupled antennas led to a large error of 17 mmHg in the pressure readout accuracy. As explained in [9], this happened because of the size and structure of the on-body 2-turns loop antenna [13]. The inner diameter of both on-body 2-turns loop antenna and implant antenna are approximately the same. Therefore, the misalignment of only 2 mm between the antennas significantly dropped the voltage at the implant terminals.

In this article, we analyze a 3D loop antenna for an on-body unit to overcome the small lateral misalignment issue. The experiment results indicate maximum improvement of 9 mmHg in the pressure readout accuracy with proposed 3D loop antenna. We also present the design steps for 3D loop antenna along with pressure readout results. Section II discusses the antenna design procedure. The fabrication and measurement setup are presented in Section III. Section IV explains the measured results and a conclusion is presented in Section V.

## II. Antenna Design Procedure

Researchers have proposed several semi-analytical or analytical solutions for the analysis of misaligned coils [14-19]. They have analyzed either lateral misalignment or both lateral and angular misalignments. In our application, we are only concerned with small lateral misalignment of the order of 2 mm because the implant is fixed and distance between the implant and the on-body unit remains constant. However, small lateral misalignment might occur if the patient removes the on-body unit and does not placed it back on the same location or it might occur if the patient walks or jogs. For an inductively coupled single turn loop antennas system, if the inner diameter is the only variable parameter of antennas and the rest of the parameters such as distance and material in between them are fixed, we can summarize as:

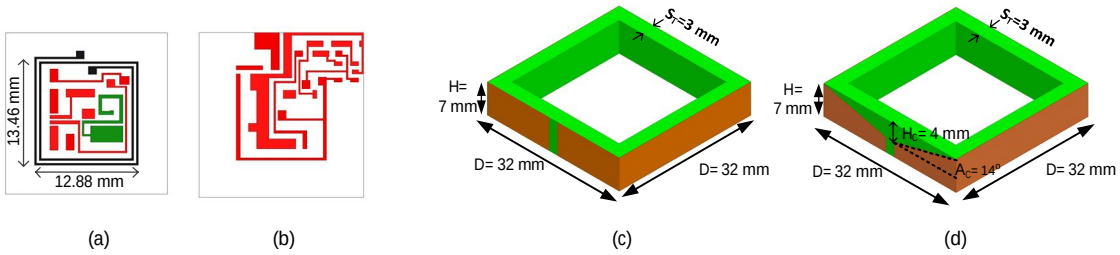


Fig. 2. (a) Front side of implant consists of 2-turns coil antenna (black), far-field antenna (green) and traces for other components (red) (b) backside of implant consists of traces for electronic components (c) initial 3D loop antenna of on-body unit (d) final 3D loop antenna of on-body unit.

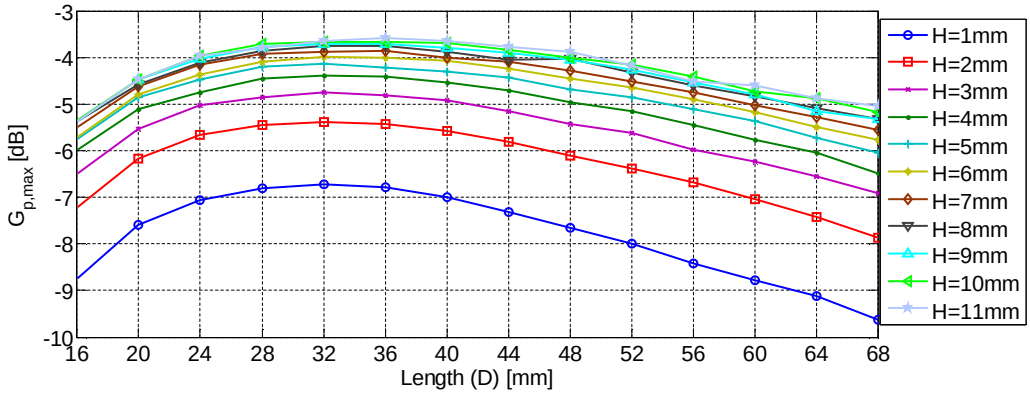


Fig. 3. Maximum link power efficiency ($G_{p,max}$) for different length (D) and height (H) at 15 MHz

1) The link power efficiency between both coupled antennas is maximum when they are centrally aligned.
2) The effect of misalignment on the link power efficiency is minimum if the radius of an on-body unit antenna is larger than the implant antenna.

This indicates that if we increase the radius of an on-body unit antenna then the effect of misalignment can be minimized but it might lower the link power efficiency. However, there are two problems. First, lower link power efficiency puts a requirement to transmit more power to activate the same implant sensor. Second, due to the human safety limit of specific absorption rate (SAR), increase in radius will decrease the maximum allowed power that we can transmit without violating the SAR limit. This happens because increase in radius will result in stronger E-field peaks generated in the tissue at both sides of the antenna input port. To the best of author's knowledge, the effect of misalignment between inductively coupled antennas on pressure readout accuracy in an ICP application has not been studied before. However, several researchers have focused on misalignment study such as in endoscopy inspection [20], in intraocular pressure measurement [21] and in electric vehicle charging [22]. Reference [23] proposed a wide-band inductive wireless link for implantable microelectronic devices. In this system, multiple frequency bands have been used for powering/communication of/with the implant. The results indicated that the proposed system can only overcome misalignment issue in one axis. Moreover, using multiple bands will result in complex design of an implant and an on-body unit. An array of on-body unit antennas proposed in [20] can be used to solve the misalignment problems but it would results in bulky and complex on-body unit. Similarly, reference [24] proposed a system embedded with supper-capacitor. The supper-capacitor provides power in case of power loss due to misalignment. The supper-capacitor with large charge storage occupies large space. Therefore, it would increase the implant size.

Thus, we have proposed a simple 3D loop antenna with the same link power efficiency and SAR value as of [13] but with a larger inner diameter. Due to the structural properties of 3D loop antenna, it shows better functionality to overcome the small misalignment issue by maintaining approximately the same overall size of the on-body unit.

### A *Wireless Link Modeling*

An anatomical human head model provided by HFSS v15 is used to model the wireless link. As shown in Fig 1(b), the on-body unit is placed at 5 mm away from the skin whereas the implant is placed in the cerebrospinal fluid (CSF). The implant is separated by 16 mm from the on-body unit. We have defined the wireless link as linear 2-port network parameters and computed the maximum link power efficiency ($G_{p,max}$) as explained in [9]. The human safety limits the maximum allowed transmission power ($P_{t,max}$) in terms of SAR. We have followed the U.S federal communications commission (FCC) regulation which limits the SAR averaged over one gram of tissue to $SAR_{max}$ = 1.6 W/kg. To calculate the $P_{t,max}$ based on $SAR_{max}$, we have followed the same SAR model explained in [9-10].

Figure 2(a-b) shows the implant front and back side. This is the same implant presented in [9]. On the front side, it has a 2-turns coil antenna that is inductively coupled with an on-body unit and a far-field antenna [25] to transmit the monitored pressure outside the skull. On the backside of the implant, there is pressure sensor to monitor the pressure. The implant is encapsulated with two layers of coating. First it is coated with biocompatible MED-2000 silicone adhesive with the total thickness of 1 mm and then with 2 µm Parylene C. Moreover, the implant is designed on a flexible polyimide substrate with the thickness of 50 $\mu$m, dielectric constant ($\varepsilon_r$) of 3.3 and tangent loss (tanδ) of 0.002.

### B. *3D Loop Antenna Optimization*

The optimum frequency for our previous design was 15 MHz. Therefore, the 3D loop was optimized for the same frequency. There were two main steps that we have followed in 3D loop antenna

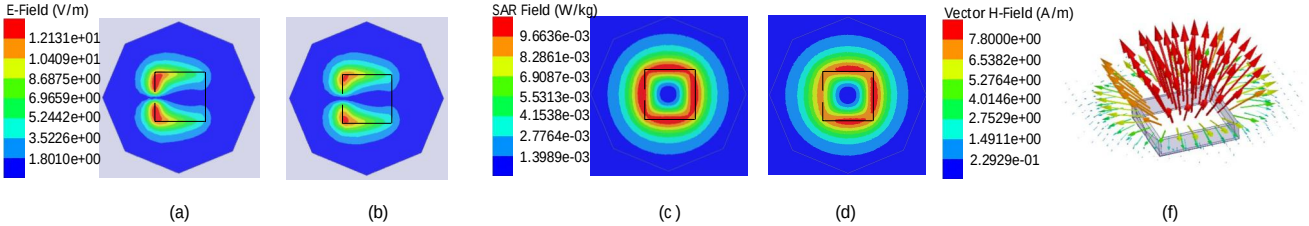


Fig. 4. (a) E-field (V/m) distribution of initial 3D loop antenna (b) E-field (V/m) distribution of final 3D loop antenna (c) local SAR (W/kg) distribution of initial 3D loop antenna (d) local SAR (W/kg) distribution of final 3D loop antenna (f) vector H-field (A/m) plot of final 3D loop antenna on the skin at 15 MHz.

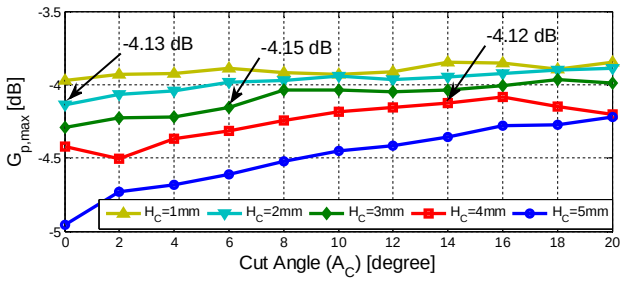


Fig. 5. $G_{p,max}$ (dB) for different values of cut-height ($H_C$) and cut-angle ($A_C$) at 15 MHz.

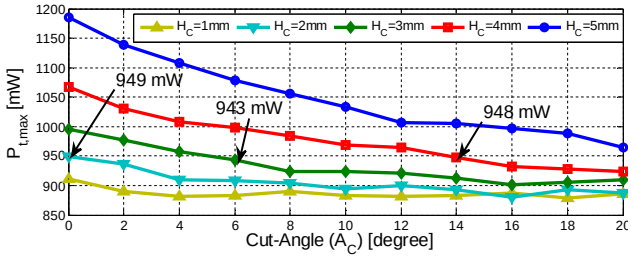


Fig. 6. $P_{t,max}$ (mW) for different values of cut-height ($H_C$) and cut-angle ($A_C$) at 15 MHz.

optimization. In the first step, we determined the length ($D$) and height ($H$) of the 3D loop antenna for maximum link power efficiency ($G_{p,max}$). Afterwards, in the second step, the cut-height ($H_C$) and cut-angle ($A_C$) were optimized to reduce the SAR with minimum effect on $G_{p,max}$. Polylactic acid (PLA) with the thickness ($S_T$) of 3 mm was printed as a substrate.

In the first step, we ran the simulation for $G_{p,max}$ by varying the $D$ of the 3D loop antenna from 16 mm to 68 mm with a step size of 4 mm and $H$ from 1 mm to 11 mm with a step size of 1 mm. Figure 3 shows the $G_{p,max}$ value for different $D$ and $H$ at 15 MHz. From Fig. 3, it is clear that for most of the curves maximum of $G_{p,max}$ occurs at $D$ = 32 mm. Moreover, with increase of $H$, $G_{p,max}$ increases. However, after $H$ = 7 mm, the increase in $G_{p,max}$ is negligible (less than 0.3 dB). Therefore, we finalized the $D$ and $H$ values as 32 mm and 7 mm respectively. Fig 2 (c) shows the initial 3D loop antenna. For initial 3D loop antenna, the $G_{p,max}$ is –3.88 dB and from the SAR model, the $P_{t,max}$ is 866 mW. This means that we can transmit 866 mW without violating the $SAR_{max}$ limit.

From [9], the 2-tuns loop antenna has $P_{t,max}$ = 940 mW. This means that 3D loop antenna has 80 mW less $P_{t,max}$ compared with the 2-turns loop antenna. This small difference is important because to activate the implant, we need to transmit around 900 mW. To reduce the SAR or increase the $P_{t,max}$, we analyzed the E-field and local SAR distribution. As skin is the closest to the on-body unit antenna, we have observed that maximum of the SAR occurred in the skin [9, 13]. Figure 4 (a) and (c) shows the E-field and local SAR distribution on the skin. The peaks of E-field are at the feeding ports. This means that the reduction in the E-field peaks can be achieved by increasing the distance between the feeding ports and the skin. As a result, the SAR decreases and $P_{t,max}$ increases. However, it reduces the $G_{p,max}$. The distance between the skin and the feeding port can be increased by changing cut-height ($H_C$) and cut-angle ($A_C$), as shown in Fig. 2(d).

To obtain the optimum values of $H_C$ and $A_C$, we ran the $G_{p,max}$ and $P_{t,max}$ simulations for different values of $H_C$ and $A_C$. Figure 5 and 6 show the simulated values of $G_{p,max}$ and $P_{t,max}$ when $H_C$ and $A_C$ are varied from 1 mm to 4 mm and 0 degree to 20 degree respectively. Both $G_{p,max}$ and $P_{t,max}$ have opposite trend with $H_C$ and $A_C$. For constant $A_C$, $G_{p,max}$ decreases with the increase in $H_C$ whereas $P_{t,max}$ increases. Similarly, for constant $H_C$, $G_{p,max}$ increases with the increase in $A_C$ whereas $P_{t,max}$ decreases. It is hard to make any conclusive decision of $H_C$ and $A_C$ values based on only $P_{t,max}$ or $G_{p,max}$ plots. Therefore, we looked both plots at the same time. For a 2-turns loop antenna [13], the $P_{t,max}$ is 940 mW. Therefore, first we selected the values of $H_C$ and $A_C$ for which $P_{t,max}$ is close to 940 mW. As highlighted in Fig. 6, at $H_C$ =2 mm, $A_C$ = 0 degree, $H_C$ =3 mm, $A_C$ = 6 degree and $H_C$ =4 mm, $A_C$ = 14 degree, the $P_{t,max}$ is 949 mW, 943 mW and 948 mW respectively. Afterward, we checked the values of $G_{p,max}$ at these three points as highlighted in Fig. 5. These values are –4.13 dB, –4.15 dB and –4.12 dB respectively. All these three values are close to each other and anyone can be selected. However, the largest value for $G_{p,max}$ amongst these is –4.12 dB corresponding to 948 mW of $P_{t,max}$. Therefore, we selected the $H_C$ = 4 mm and $A_C$ = 14 degree. Figure 1 (d) shows the final 3D loop antenna shape with optimized dimensions. The final 3D loop antenna has $G_{p,max}$ = –4.12 dB and $P_{t,max}$ = 948 mW. Although $G_{p,max}$ decreases from –3. 8 dB to –4.12 dB, $P_{t,max}$ increases from 881 mW to 948 mW. This 0.3 dB decrease in $G_{p,max}$ is small. Moreover, the final 3D loop antenna provides nearly equal $G_{p,max}$ with the 2-turns loop antenna (–4.10 dB [13]).

### C. Simulation Results

Figure 7 shows the simulated $G_{p,max}$ of the final 3D loop antenna for different frequency. After 10 MHz the $G_{p,max}$ has stable trend up to 25 MHz. This means that there is broad optimum frequency range in terms of maximum $G_{p,max}$. However, as stated before, the implant has already been designed at 15 MHz; therefore, we are interested in 15MHz. Figure 4 (b) and (d) show the E-field and local SAR distribution of final 3D loop antenna. It is clear that E-field peaks and local SAR intensity reduce due to optimization of $H_C$ and $A_C$ values.

The antenna with a bigger diameter has stable H-field distribution in larger area compared with the antenna with a smaller diameter. Therefore, due to this property, the antenna with a bigger diameter can overcome the effect of misalignment better. To verify the performance of our 3D loop antenna in terms of stable H-field

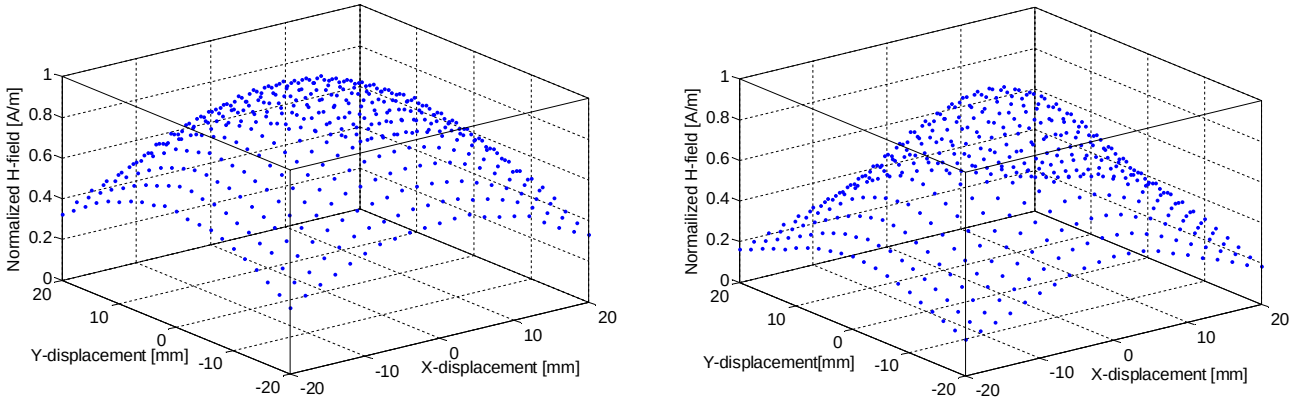


**(a)** **(b)**

Fig. 8. Normalized H-field distribution at 16 mm away from the antenna in a plane parallel to (a) 3D loop antenna (b) 2-turns loop antenna of [13].

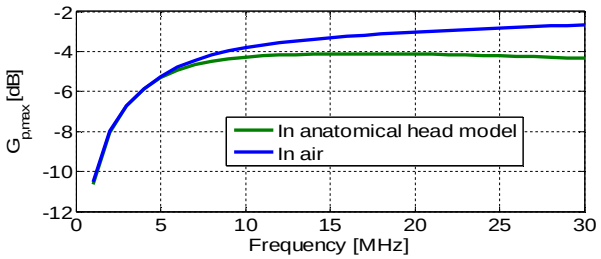


Fig. 7. Simulated $G_{p,max}$ (dB) in the anatomical head model and in the air for 3D loop antenna.

distribution, we have plotted the vector H-filed (A/m) and normalized H-field distribution in Fig. 4(f) and Fig. 8 respectively. The vector H-field was plotted perpendicular to the skin and the normalized H-field distribution was extracted in a plane parallel to the antenna at 16 mm away from it. From Fig. 4(f), it is clear that H-field vectors have uniform field distribution within the loop inner area. Figure 8 also shows the normalized H-field for the 2-turns loop antenna [13]. H-field values were extracted from X = –20 mm to +20 mm and Y= –20 mm to + 20 mm, where X= 0 mm and Y = 0 mm is the center of the antenna and at 16 mm away. From Fig. 8, it is clear that the rate of change of H-field with respect to X- and Y-displacement is smaller for 3D loop antenna compared with the 2-turns loop antenna [13].

## III. Fabrication and Measurement Setup

### A. Substrate Printing

The prototype of the substrate was printed using a Prenta Duo 3D printer with two 1.75 mm nozzles. The printer allows the manufacturing of complex 3D models using layer by layer deposition of versatile materials like Acrylonitrile-butadiene styrene (ABS) and polylactic acid (PLA). The main advantage offered by 3D printing technology is the ability to fabricate customized substrate structures (thickness, filling, shape) with varying electrical (permittivity) and mechanical properties (weight, flexibility). PLA was used as the substrate material for the antenna because it offers the benefit of low cost and light weight. To print the substrate material (PLA), the printing speed was set at 40 mm/s with a nozzle printing temperature of 215-220 °C, and a print bed temperature of 60 °C. 100 % infill was used to have a solid 3D antenna structure.

### B. Fabrication of 3D Loop Antenna and Matching Circuit

After substrate printing, copper tape was used to fabricate the 3D loop antenna. First, copper tape with the width of 7 mm was attached to the substrate. Afterwards, copper tape was cut at feeding port with respect to the $H_C$ and $A_C$ values.

An LC matching network configuration was used to match the antenna to 50 Ω. ANSYS designer was used to simulate the matching network. A capacitor of 1120 pF was used in parallel to an inductor of 39 nH. The effect of parasitic elements on the simulation was also observed by adding the parasitic element values in the simulation. After the simulation, the matching network was fabricated and attached to the antenna. Figure 9 shows the 3D loop antenna with a matching network.

### C. Measurement Setup

Three different measurements were performed to verify the performance of the 3D loop antenna. These included S-parameter measurement, pressure readout measurement and misalignment measurement. We were mainly interested in misalignment measurement. However, S-parameter measurement was done to verify the 3D loop antenna performance alone. Moreover, pressure readout measurement was conducted to assess the pressure monitoring system accuracy (shift in frequency per 1 mmHg) with 3D loop antenna. Without knowing the shift in frequency of the received signal per 1 mmHg, we cannot calculate the error induced due to misalignment. Therefore, first we performed the S-parameter measurement to verify the 3D loop antenna performance alone, then performed the pressure readout experiment and afterward, studied the misalignment effect on the pressure readout accuracy.

As highlighted in Fig 1 (a), there are two wireless links in our proposed pressure monitoring system. First is the inductive link to power the implant and second is the far-field link to transmit the monitored pressure outside the skull. For an inductive link, the material in between the coupled antennas is important whereas for a far-field link, the material surrounding the far-field antenna [25] is important. The far-field antenna [25] was designed for human head; therefore, the environment around it should be close to human head environment for its normal operation.

Figure 9 shows the measurement setup. The implant was placed in a glass bottle filled with COMOSAR Head Liquid. The liquid followed the IEEE standard for head properties at 2.45 GHz: $\varepsilon_r$ = 39.2 and $\sigma$ = 1.8 S/m. The measured properties of COMOSAR Head Liquid at 2.45 GHz were $\varepsilon_r$ = 38.58 and $\sigma$ = 1.88 S/m. There was a gap of 16 mm (10 mm air + 4 mm glass + 2 mm COMOSAR Head Liquid) between the coupled antennas. Moreover, the temperature of the liquid was 24 ºC at the time of measurement.

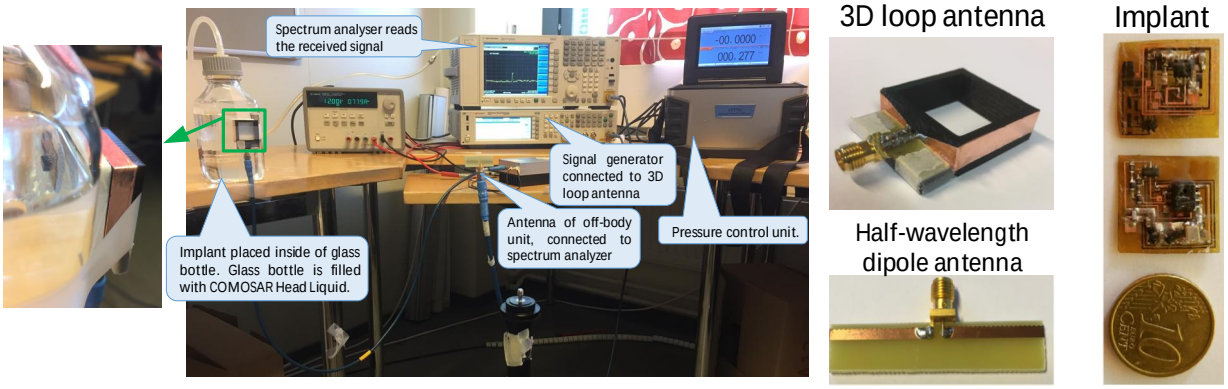


Fig. 9. Measurement setup, fabricated implant, half-wavelength dipole antenna and 3D loop antenna.

For far-field link operation, we have used the COMOSAR Head Liquid. The liquid, mimicking the head properties, presence in the surrounding of the far-field antenna helped to operate the antenna normally. However, to make the measurement simple, in the inductive link we used an air gap between the coupled antennas. As shown in the Fig 7, the simulation results in the air presented good approximation to the anatomical model. At our interested frequency of 15 MHz, there is less than 1 dB difference in $G_{p,max}$ between the anatomical head model and in the air.

The 3D loop antenna was connected to the signal generator. As the 3D loop antenna was fed with input power of 31 dBm, it activated the implant. After the activation, the implant started monitoring the pressure and transferred it to the off-unit half-wavelength dipole antenna at ISM band. The half-wavelength antenna was placed at 1 m distance from the glass bottle and was connected to the spectrum analyzer. The received signal of the half-wavelength dipole antenna was displayed on the spectrum analyzer. Moreover, the pressure inside the glass bottle was maintained through ADT761 pressure controlling device.

## IV. Measurement Results and Discussion

### A. S-parameter Measurement

S-parameters were measured through a vector network analyzer (VNA). An SMA connector is connected to the implant coil antenna. Port 1 of VNA was connected to 3D loop antenna and port 2 to the implant. There was an air gap of 16 mm between the 3D loop antenna and the implant coil antenna. Moreover, both were centrally aligned. The measured S-parameters at 15 MHz were; S11 = –5.1 dB, S22 = –4.0 dB and S21= S12 = –14.0 dB. This means that overall power transfer efficiency of the system was –14.0 dB (3.97%).

We estimated the $G_{p,max}$ from measured S-parameters. The $G_{p,max}$ was estimated by compensating the matching circuit loss. The simulated and measured $G_{p,max}$ were –3.3 dB and –3.7 dB respectively. Moreover, the loss induced due to the matching network was 6.5 dB. The loss is high due to parasitic elements as explained in [10].

### B. Pressure Readout Experiment

In this experiment, the pressure inside the glass bottle was varied and shift in the frequency of the received signal was observed. The pressure inside the glass bottle was increased/decreased through ADT761 pressure controlling device. The purpose of this experiment was to calculate the shift in frequency per 1 mmHg. This was going to be used in calculating the pressure readout error during misalignment measurement.

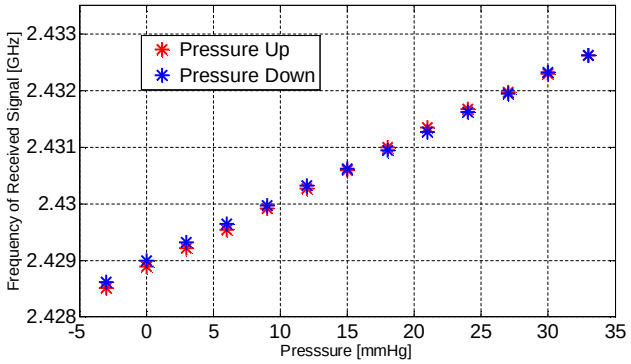


Fig. 10. Frequency of the received signal with pressure variation in pressure readout experiment.

Figure 10 shows the pressure readout experiment results. With the change of pressure, the frequency of received signal changes. Pressure was varied in Up and Down directions from –3 mmHg to 33 mmHg with a step size of 3 mmHg. There was total 4.05 MHz shift in the frequency of the received signal corresponding to 36 mmHg change in the pressure. This means that there was 112 kHz shift in the frequency of the received signal corresponding to 1 mmHg. Overall, the pressure monitoring system has similar performance as reported in [9].

### C. Misalignment measurement

In this measurement, we study the effect of misalignment on the pressure readout accuracy. The distance between implant and 3D loop antenna, material between them, the external pressure and feed power to the 3D loop antenna were kept constant. However, only 3D loop antenna was moved on a rectangular coordinate axis from X = –2 mm to X = +2 mm and Y = –2 mm to Y = +2 mm with a step size of 2 mm. There were total 8 points on the rectangular coordinate axis.

Figure 11 shows the pressure readout error induced due to misalignment. As the both implant and 3D loop antenna were misaligned, the voltage at the sensor terminals dropped and as a result the frequency of the received signal shifted to lower value even at the same pressure. Figure 11 shows the shift in the frequency of the received signal along with pressure readout error. The negative sign shows that the signal frequency shifted to lower values compared with the centrally aligned case.

The error in pressure readout was calculated by dividing the shift in frequency to 112 kHz. For example, at X = +2 mm and Y = 0 mm, the frequency of the received signal was shifted by –350 kHz. This means that there would be extra –4 mmHg (–350/112 = –3.1 and rounded off to next whole number which is –4) error induced in pressure readout due to misalignment. In studied misalignment cases, the maximum error was –8 mmHg.

Figure 11 also presents the pressure readout error due to the 2-turns loop antenna reported in [9] for a comparison with our proposed 3D loop antenna. It is clear that system shows maximum improvement of 9 mmHg in pressure readout accuracy with proposed 3D loop antenna. The proposed 3D loop antenna is simple in design, small in size, low in cost and easy to fabricate. Moreover, with the same gain and the same SAR values as of the 2-turns loop antenna, the proposed 3D loop antenna significantly reduces the pressure readout error due to misalignment.

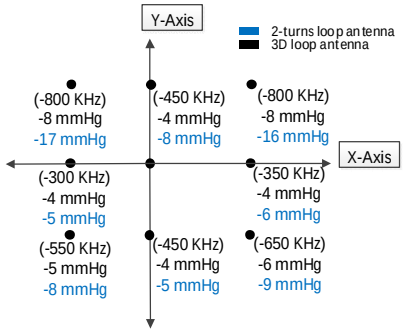


Fig. 11. Misalignment results. Shift in the frequency of the received signal due to misalignment effect. Pressure readout error of 3D loop antenna. Also pressure readout error of 2-turns loop antenna presented in [9].

## V. Conclusion

We presented a simple, low cost and small size 3D loop antenna to overcome the pressure readout error caused due to misalignment between the coupled antennas in an intracranial pressure (ICP) monitoring system. There was maximum of 9 mmHg improvement in pressure readout error with the proposed 3D loop antenna. Moreover, the new antenna maintained the same maximum link power efficiency ($G_{p,max}$) with the similar specific absorption rate (SAR) compared with previously reported 2-turns loop antenna [13]. However, the 3D loop antenna is able to overcome the error caused due to misalignment. Our next step is to perform the drift study of our proposed ICP monitoring system by utilizing newly designed 3D loop antenna.

## References

[1] M. Smith, “Monitoring intracranial pressure in traumatic brain injury,” *Anesth. Analg*., vol. 106, no. 1, pp. 240–248, 2008.

[2] X. Hu, *et al*., “Estimation of hidden state variable of the intracranial system using constrained nonlinear Kalman filters,” *IEEE Trans. Biomed. Eng*., vol. 54, no. 4, pp. 597¬610, Apr. 2007.

[3] L. A. Steiner, P. J. D. Adnrews, “Monitoring the injured brain: ICP and CBF,” *Br. J. Anesth*., vol. 97, no. 1, pp. 26–38, May 2006.

[4] P. H. Raboel, J. Bartek, M. Andresen, B. M. Bellander, B. Romner, “Intracranial pressure monitoring: invasive versus non-invasive methods – a review,” *Crit. Care Res. Pract*., vol. 2012, article ID: 950393, Mar. 2012.

[5] U. Kawoos, M.-R. Tofighi, R. Warty, F. A. Kralick, A. Rosen, “In-vitro and in-vivo trans-scalp evaluation of an intracranial pressure implant at 2.4 GHz,” *IEEE Trans. Microw. Theory Techn*., nol. 56, no. 10, pp. 2356–2365, Oct. 2008.

[6] K. Aquilina, M. Thoresen, E. Chakkarapani, I. K. Pople, H. B. Coakham, and R. J. Edwards, “Preliminary evaluation of a novel intraparenchymal capacitive intracranial pressure monitor: Laboratory investigation,” *J. Neurosurg*., vol. 115, no. 3, pp. 561–569, 2011.

[7] L. Y. Chen, B. C. K. Tee, A. L. Chortos et al., “Continuous wireless pressure monitoring and mapping with ultra-small passive sensors for health monitoring and critical care,” *Nature Commun.*, vol. 5, article 5028, 2014.

[8] Mohammad H. Behfar, E. Moradi, T. Björninen, L. Sydänheimo, and L. Ukkonen, “Biotelemetric wireless intracranial pressure monitoring: an in vitro study,” *Intl. J. Antennas and Propag*., vol. 2015, article ID 918698, 10 pages, 2015.

[9] M. W. A. Khan, L. Sydänheimo, L. Ukkonen, T. Björninen, “Inductively powered pressure sensing system integrating a far-field data transmitter for monitoring of intracranial pressure,” *IEEE Sensors Journal*, vol. 17, no. 7, pp. 2191-2197, Apr. 2017.

[10] M. W. A. Khan, T. Björninen, L. Sydänheimo, and L. Ukkonen, “Remotely powered piezoresistive pressure sensor: toward wireless monitoring of intracranial pressure,” *IEEE Microw. Wireless Compon. Lett.*, vol. 26, no. 7, pp. 549–551, June 2016.

[11] J. Zhong, M. Dujovny, H. K. Park, E. Perez, A. R. Perlin, and F. G. Diaz, “Advances in ICP monitoring techniques, ” *Neurological research* 25.4, pp. 339-350, Jun. 2003.

[12] M. W. A. Khan, M. Rizwan, L. Sydänheimo, Y. Rahmat-Samii, L. Ukkonen, T. Björninen, “Effect of temperature variation on remote pressure readout in wirelessly powered intracranial pressure monitoring system,” *IEEE EMBC*, pp. 1728-1731 , 2017.

[13] M. W. A. Khan, T. Björninen, L. Sydänheimo, L. Ukkonen, “Characterization of two-turns external loop antenna with magnetic core for efficient wireless powering of cortical implants,” *IEEE Antennas Wireless Propag. Lett.*, vol. 15, pp. 1410–1413, Apr. 2016.

[14] F. C. Flack, E. D. James, and D. M. Schlapp, “Mutual inductance of air-cored coils: Effect on design of radio-frequency coupled implants,” *Med. Biol. Eng. Comput.* , vol. 9, pp. 79–85, 1971.

[15] E. S. Hochmair, “System optimization for improved accuracy in transcutaneous signal and power transmission,” *IEEE Trans. Biomed. Eng*., vol. BME-31, no. 2, pp. 177–186, 1984.

[16] M. Soma, C. D. Galbraith, and R. White, “Radio-frequency coils in implantable devices: Misalignment analysis and design procedure,” *IEEE Trans. Biomed. Eng.* , vol. BME-34, no. 4, pp. 276–282, 1987.

[17] S. Babic and C. Akyel, “Improvement in calculation of the self- and mutual inductance of thin-wall solenoids and disk coils,” *IEEE Trans. Magn.* , vol. 36, no. 4, pp. 1970–1975, Jul. 2000.

[18] S. Babic and C. Akyel, “Calculating mutual inductance between circular coils with inclined axes in air,” *IEEE Trans. Magn*., vol. 44, no. 7, pp. 1743–1750, Jul. 2008.

[19] K. Fotopoulou and B. W. Flynn, "Wireless Power Transfer in Loosely Coupled Links: Coil Misalignment Model," *IEEE Transactions on Magnetics*, vol. 47, no. 2, pp. 416-430, Feb. 2011.

[20] T. Sun, *et al.*, "A Two-Hop Wireless Power Transfer System With an Efficiency-Enhanced Power Receiver for Motion-Free Capsule Endoscopy Inspection," *IEEE Transactions on Biomedical Engineering*, vol. 59, no. 11, pp. 3247-3254, Nov. 2012.

[21] A. E. Rendon-Nava, *et al.*, “Study of the Effect of Distance and Misalignment between Magnetically Coupled Coils for Wireless Power Transfer in Intraocular Pressure Measurement,” *The Scientific World Journal*, vol. 2014, Article ID 692434, 11 pages, 2014.

[22] K.A. Kalwar, S. Mekhilef, M. Seyedmahmoudian, B. Horan, "Coil Design for High Misalignment Tolerant Inductive Power Transfer System for EV Charging." *Energies* 9, no. 11: 937, 2016.

[23] M. Ghovanloo and S. Atluri, "A Wide-Band Power-Efficient Inductive Wireless Link for Implantable Microelectronic Devices Using Multiple Carriers," *IEEE Transactions on Circuits and Systems I: Regular Papers*, vol. 54, no. 10, pp. 2211-2221, Oct. 2007.

[24] A. P. Hu, I. L. W. Kwan, C. Tan, Y. Li, "A wireless battery-less computer mouse with super capacitor energy buffer", *IEEE Conf. Ind. Electron. Appl. (ICIEA)*, pp. 2024-2029, May 2007.

[25] M. W. A. Khan, E. Moradi, L. Sydänheimo, T. Björninen, Y. Rahmat-Samii, L. Ukkonen, “Miniature co-planar implantable antenna on thin and flexible platform for fully wireless intracranial pressure monitoring system,” *Intl. J. Antennas Propag.*, vol. 2017, Article ID 9161083, 9 pages, 2017.